Article

Experimental Study on the Strength Distribution and Pore Distribution of Industrial Pellet and DRI

Zhengjian Liu [1], Shaofeng Lu [1], Yaozu Wang [2,3,*] and Jianliang Zhang [1,*]

[1] School of Metallurgical and Ecological Engineering, University of Science and Technology Beijing, Beijing 100083, China; liuzhengjian@ustb.edu.cn (Z.L.); wshjshwzh@126.com (S.L.)

[2] School of Intelligence Science and Technology, University of Science and Technology Beijing, Beijing 100083, China

[3] Institute of Artificial Intelligence, University of Science and Technology Beijing, Beijing 100083, China

* Corresponding author. E-mail: yaozuwang@ustb.edu.cn (Y.W.); zhang.jianliang@hotmail.com (J.Z.)

ABSTRACT: Against the backdrop of the "dual-carbon" goals driving the steel industry's transition toward hydrogen metallurgy, the hydrogen-based shaft furnace process has emerged as a focal point due to its low-carbon emissions. This study employs compression testing, mercury intrusion porosimeter, and industrial computed tomography characterization to compare the mechanical properties and pore structures of industrial pellets and direct reduced iron (DRI). The results show that the compressive strength and mass specific breakage energy of DRI are lower than those of pellets, and the breakage characteristic parameters at the same particle size are lower, making it more prone to breakage; the compressive strength of both increases with the increase of particle size, the mass specific breakage energy decreases with the increase of particle size, and the strength growth rate of pellets is faster. In terms of pore structure, pellets are mainly composed of uniform macropores of 3428 nm with a porosity of 22.3%; DRI has a porosity of 48.8%, mainly composed of 3431 nm macropores and 831 nm micropores, with a low tortuosity index, which is conducive to gas diffusion. This study provides parameters and theoretical basis for modeling of burden movement and crushing in shaft furnace.

Keywords: Ironmaking; Pellet; DRI; Compressive strength; Breakage energy; Porosity

1. Introduction

Under the "Carbon neutrality" and "Carbon peaking" goals, the pressure on the steel industry to reduce carbon emissions is increasing, and it is actively seeking a transition from carbon metallurgy to hydrogen metallurgy [1,2]. As an emerging non-blast furnace ironmaking process, the hydrogen-based shaft furnace process has gradually become the focus of the steel industry due to its advantages, such as high hydrogen consumption and low carbon emissions [3–5]. In the production process of the shaft furnace, the stable and smooth production of qualified direct reduced iron (DRI) is the key to the hydrogen-based shaft furnace process. However, in actual industrial production, DRI discharged from the shaft furnace sometimes breaks [6], indicating that during the downward movement of the burden in the shaft furnace, the burden continuously undergoes impacts due to collisions between burden particles and between burden and the furnace wall, eventually exceeding its strength and causing breakage. The broken small particles of burden will fill the pores of the moving bed, reducing the permeability of the bed layer and affecting the distribution of gas flow, which may lead to production problems such as reduced metallization degree, burden blockage, and decreased yield, thereby hindering the stable, high-yield, and smooth operation of the shaft furnace. Moreover, in the subsequent electric arc furnace (EAF) process, broken DRI can cause uneven feed flow and unstable arcs, thereby reducing the overall efficiency of the EAF. The main cause of this phenomenon is the breakage of the burden due to the reduction of its strength during the reduction process.

Previous studies have mainly focused on mechanical property experiments and DEM simulations of unreduced pellets. Barrios et al. [7] systematically calibrated parameters such as the restitution coefficient, static friction coefficient,

and rolling friction coefficient of pellets through single-ball impact tests, friction tests, and rolling angle measurements. The study compared the effects of the single-sphere model and the overlapping sphere model on pellet motion simulation, and the results showed that the overlapping sphere model can more realistically reflect the rolling and collision behaviors of non-spherical particles. In addition, the effectiveness of the parameters was verified through slump tests and tumbling tests. Subsequently, Barrios et al. [8] conducted single-particle breakage tests, particle bed breakage tests, and DEM breakage simulations on iron ore pellets. The single-particle breakage tests were used to obtain material breakage parameters, and the DEM simulation results showed good agreement with the experiments regarding force-displacement curves and specific breakage energy. Tavares et al. [9] focused on the body crushing mechanism of pellets under impact.Through drop-weight tests and compression tests, they found that the pellet crushing probability is directly related to the normal component of impact energy, which a gamma distribution can describe, and a significant size effect exists (the larger the particle size, the lower the crushing energy). Meanwhile, it was found that the model parameter γ of different pellet samples varies between 6.9 and 10.5, but does not change significantly with pellet size. The influence of impact angle on crushing was verified, and the energy distribution during the collision process was analyzed by combining DEM simulations. Cavalcanti et al. [10] developed a pneumatic gun device to simulate high-energy impacts, systematically analyzing the effects of different impact angles (30°–90°) and surface materials (steel, aluminum, rubber) on pellet crushing. The results show that the bulk crushing probability only depends on the normal impact energy. At the same time, the mass loss of surface damage is related to the tangential component of impact energy, and a modified wear model was proposed. Boechat et al. [11] conducted DEM simulations on the MINIMOD MIDREX shaft furnace using the material breakage parameters of unreduced pellets. The compressive force and collision energy distributions in various regions of the furnace under different production capacities were analyzed. The simulated regions were not based on a complete shaft furnace but divided into four parts for separate simulation. Although the DEM simulations did not include burden breakage and wear, according to the collision energy data obtained from the simulations, the model proposed by Cavalcanti [12] was used to predict that the fine generation ratio in the reduction zone during normal operation was 3.4%, which could increase to 4.6% when production was increased. Boechat et al. [13] reduced pellets to different reduction degrees and then carried out experiments such as cold compression strength tests and drop tests. The results showed that with the increase in reduction degree, the cold compression strength decreased significantly, and the mass loss of surface breakage caused by the same impact energy increased. Based on the model in reference [11] and combined with the fine generation coefficients of pellets with different reduction degrees, the fine generation ratio in the furnace was predicted to be 5.7%. Petit et al. [14] proposed a numerical simulation method that integrates DEM, CFD, continuum damage mechanics, and particle dynamics theory. This approach first uses DEM to simulate the MINIMOD MIDREX shaft furnace to obtain collision energy data of the burden. Then, the CFD-KTGF model is employed to treat the particle phase as a pseudo-fluid for simulation to reduce computational load. The study investigates the generation of burden fragments during the reduction process and their effects on the velocity and pressure fields of the reducing gas.

Compression tests were performed on industrial pellets and DRI, and fitting equations obtained breakage parameters, providing corresponding parameters for modeling the movement and breakage processes of burdens in hydrogen-based shaft furnaces. Meanwhile, differences between pellets and DRI were compared in aspects such as sample porosity and spatial distribution of pore sizes, to explain the distinctions in breakage properties between pellets and DRI.

2. Experiment

2.1. Experimental Materials

The pellets used in the experiment were those used by the direct reduction plant, the DRI was produced by the ENERGIRON-ZR process, with a metallization degree of 94% and a carbon content of 2.76%, and their main chemical compositions are shown in Table 1.

Table 1. Main chemical compositions of pellet and DRI used in the experiment.

Composition, wt%	TFe	FeO	SiO$_2$	CaO	Al$_2$O$_3$
Pellet	67.45	0.61	1.27	0.29	0.52
DRI	89.72	5.38	2.95	0.64	0.69

Four different particle size distributions were selected for the strength distribution study of pellets and DRI, respectively. Four particle size distributions chosen for pellets were: 10–12.5 mm, 12.5–14 mm, 14–16 mm, and 16–20 mm; those for DRI were: 8–10 mm, 10–12.5 mm, 12.5–14 mm, and 14–16 mm. The selected pellets and DRI have different particle size ranges, and the DRI has a smaller particle size range. This discrepancy arises because pellet degradation during the reduction process reduces the DRI particle size. The particle size ranges for the pellets used in the plant and the produced DRI are shown in Table 2.

Table 2. Particle size distribution of pellets and DRI.

Pellet Size Range, mm	Percentage, %	DRI Size Range, mm	Percentage, %
25–16	4.7	25–16	4.1
16.5–12.5	58.6	16–10	73.3
12.5–10	29.3	10–6.3	19.3
10–5	6.5	6.3–3.15	2.8
<5	0.9	<3.15	0.5

The pellets and DRI used in the experiment had no obvious large cracks on their surfaces and no significant structural defects. The typical shapes of the pellets and DRI are shown in Figure 1.

(a)   **(b)**

Figure 1. Samples used in the experiment, (**a**) pellets; (**b**) DRI.

2.2. Experimental Method

An electronic universal testing machine was used to perform uniaxial compression and repeated compression tests on industrial pellets and DRI to obtain force-displacement curves. The compression rate was 0.5 mm/min, sufficiently low to neglect inertial effects. Due to the high rigidity of the loading device, its deformation could be ignored. The force-displacement curves during loading were recorded

The number of uniaxial compression tests for each particle size was more than 30. After obtaining the force-displacement curves from the uniaxial compression tests, the maximum force before breakage was taken as the compressive strength (i.e., breaking force) of the pellets and DRI. For the repeated compression tests, each compression applied a strain of 5%, and the process was repeated until particle breakage occurred.

To compare the structural differences between pellets and DRI, mercury intrusion porosimeter (MIP) determined the overall pore size distribution using an AutoPore IV 9520 porosimeter (Micromeritics, Norcross, GA, USA). During the measurement, the pressure was increased from 0.49 psia to 32,992.46 psia

The internal pore distribution of samples was characterized using an FF35 X-ray CT scanner (YXLON, Tokyo, Japan). The scanner employed a micro-focus X-ray source to perform 360° scans of the samples, with a scanning time of approximately 10 min. The tube voltage during the scanning process is 160 kV and the tube current is 120 μA. Three-dimensional reconstruction was conducted using visualization software (VG Studio MAX, Volume Graphics, Heidelberg, Germany); the reconstruction algorithm uses Feldkamp, yielding a 3D model with a resolution of $16.22 \times 16.22 \times 16.22$ μm. The 3D pore distributions of pellets and DRI were obtained through analysis of the scanning results.

The particle size of pellets and DRI tested using MIP and CT was 12.5–16 mm, the range with the largest proportion of pellets and DRI size distribution.

3. Results and Discussion

3.1. Strength Distribution

The typical force-displacement curves of pellets and DRI are shown in Figure 2. Figure 2a shows that the pellet exhibits a flat region at the initial loading stage, representing a centroid stabilization period with minimal force variation. This stage primarily involves the adjustment of irregular particle positions. Subsequently, it enters the elastic deformation stage, where the experimental device continuously increases the compression on the particle. During this process, the edges and corners at the contact area between the particle surface and the indenter are found to fracture, resulting in local minor breakage, as indicated by the blue circle in Figure 2a, which corresponds to the local edge peeling stage. As the force continues to increase, when the experimental force reaches its maximum, the particle undergoes complete fracture, which is reflected in the force-displacement curve as a sudden drop in load, as shown by the red circle in Figure 2a. This stage is the complete fracture period, where the pellet breaks into several small fragments, some of which may even splash out. The compressive strength of the pellet is the maximum force value (F_c) in the force-displacement curve, and the corresponding displacement (δ_c) is the displacement at breakage.

Figure 2b shows the force-displacement curve of DRI. It can be seen that DRI also exhibits a flat region at the initial loading stage, followed by the elastic deformation stage, and breakage occurs at the position indicated by the red circle. However, the difference between DRI and pellets lies in the area shown by the green box. After DRI breaks, large-volume fragments do not splash but collapse and stack on each other. Therefore, the force shows a fluctuating decline in the green box rather than a sudden drop after breakage.
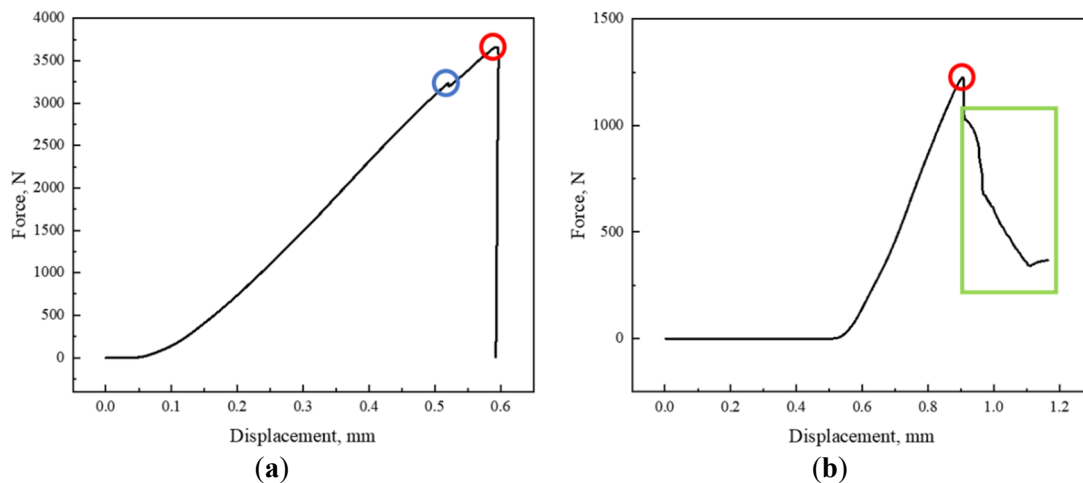

(a)   **(b)**

Figure 2. Typical force-displacement curves: (**a**) Pellet, 14–16 mm, 7.0094 g; (**b**) DRI, 12.5–14 mm, 4.4403 g. (The blue circle indicates that the particles have small local fractures, the red circle indicates that the particles are completely broken, and the green frame indicates that the particles are stacked after they are broken).

Through the force-displacement curve, the specific breakage energy can be calculated. The specific breakage energy (E_s) is the energy required to break a unit mass of the sample (J/kg), as shown in Equation (1).

$$E_s = \frac{\int_0^{\delta_c} F \ d\delta}{m}$$

(1)

where F represents the load force during uniaxial compression (N), δ is the displacement during compression (mm), δ_c is the displacement corresponding to DRI breakage, and m is the particle mass (g).

For a finite number of samples, the particle breakage probability can be calculated using the probability estimation factor (P), as shown in Equation (2). Here, N is the total number of experimental samples, and i is the rank of a specific particle strength in the sequence after arranging the strength data of all specimens in ascending order.

$$P = \frac{i - 0.5}{N}$$

(2)

The Lognormal model is employed to fit the data when defining the breakage probability $P(F)$ using compressive strength.

$$P(F) = \frac{1}{2}\left[1 + \text{erf}\left(\frac{\ln F_C - \ln a_F}{\sqrt{2\sigma_F{}^2}}\right)\right] \tag{3}$$

when defining the breakage probability $P(E)$ using specific breakage energy, the Lognormal model improved by Tavares [15] is employed to fit the data.

$$P(E) = \frac{1}{2}\left[1 + \text{erf}\left(\frac{\ln E^* - \ln a_E}{\sqrt{2\sigma_E{}^2}}\right)\right] \tag{4}$$

$$E^* = \frac{E_{\max} E}{E_{\max} - E} \tag{5}$$

where σ^2 represents the variance, α is the fitting parameter, F_C is the compressive strength, E^* is an expression related to E, E is the specific breakage energy, and $E_{\max}/\alpha_E = 4$.

The breakage probability $P(F)$ of pellets with different particle sizes and the fitting curves based on compressive strength are shown in Figure 3. It can be observed that as the pellet size increases, the compressive strength corresponding to the same breakage probability gradually increases.
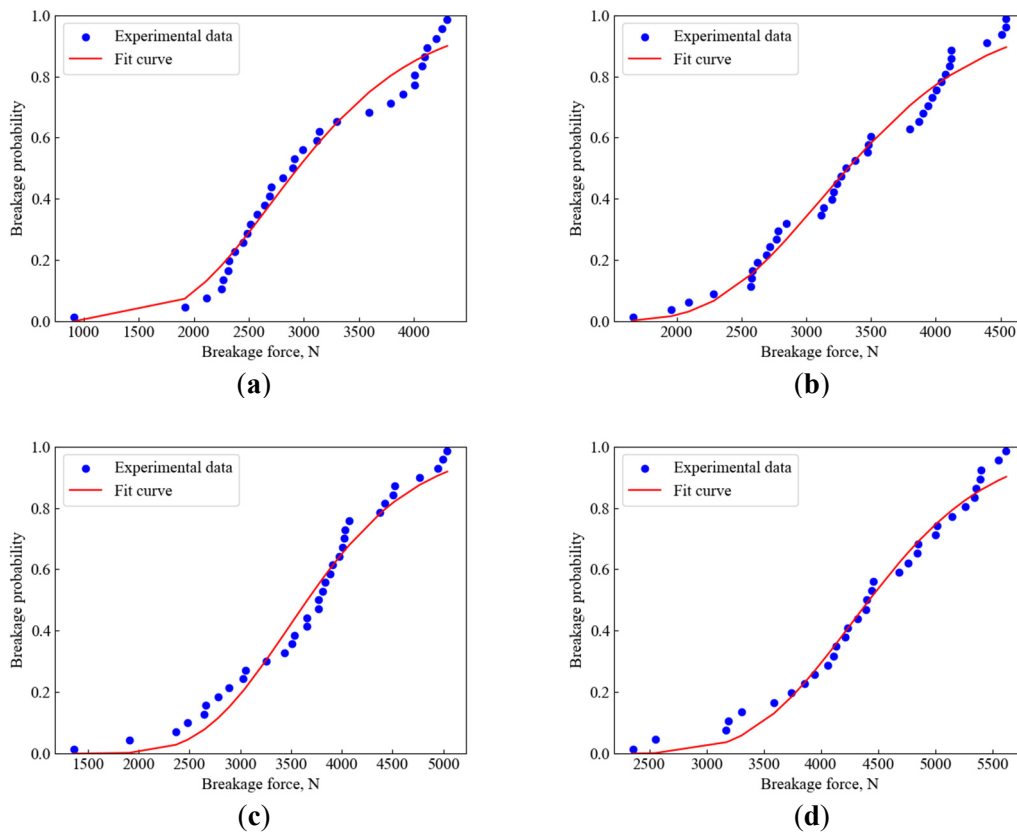

Figure 3. Distribution of breakage probability and compressive strength for pellets with different particle sizes: (**a**) 10–12.5 mm; (**b**) 12.5–14 mm; (**c**) 14–16 mm; (**d**) 16–20 mm.

The breakage probability $P(E)$ of pellets with different particle sizes and the fitting curves based on specific breakage energy are shown in Figure 4. It can be observed that for the same breakage probability, the larger the pellet size, the lower the corresponding specific breakage energy.
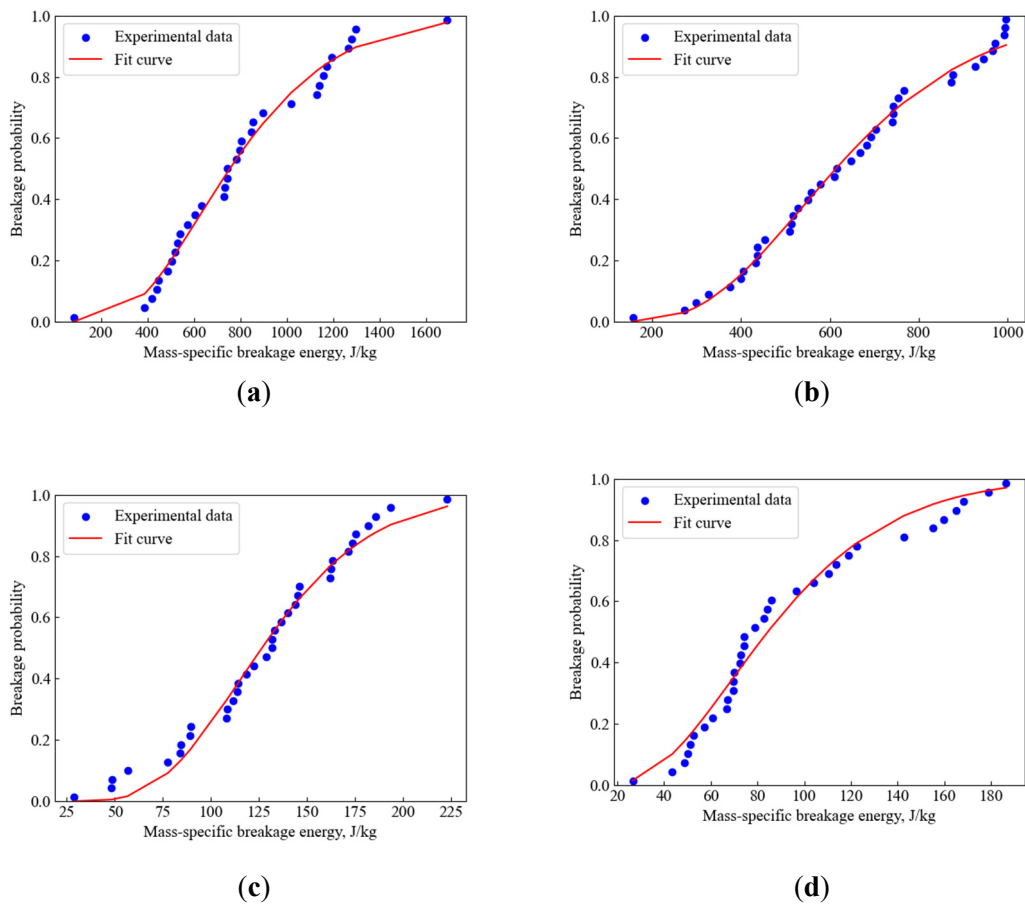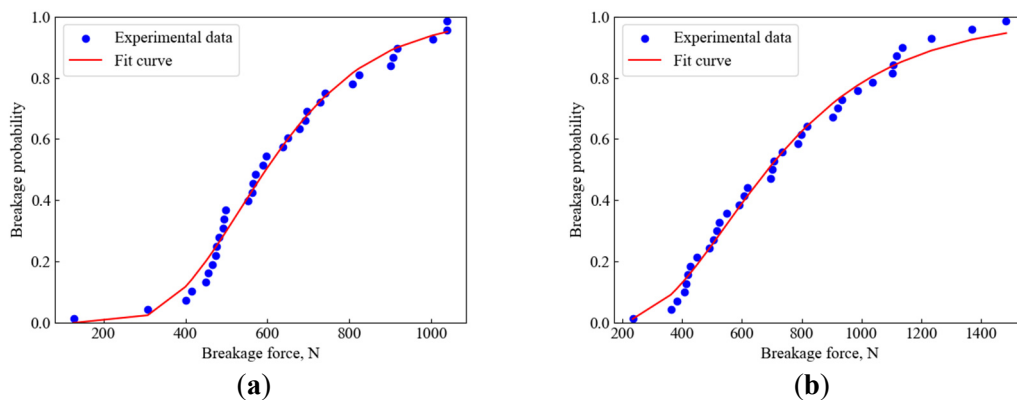
Figure 4. Distribution of breakage probability and specific breakage energy for pellets with different particle sizes: (**a**) 10–12.5 mm; (**b**) 12.5–14 mm; (**c**) 14–16 mm; (**d**) 16–20 mm.

The breakage probability $P(F)$ of DRI with different particle sizes and the fitting curves based on compressive strength are shown in Figure 5. Similar to pellets, it can be observed that the compressive strength corresponding to the same breakage probability increases with the increase in DRI particle size. Compared with Figure 3, under the same particle size and breakage probability, the breaking force of pellets is greater than that of DRI.
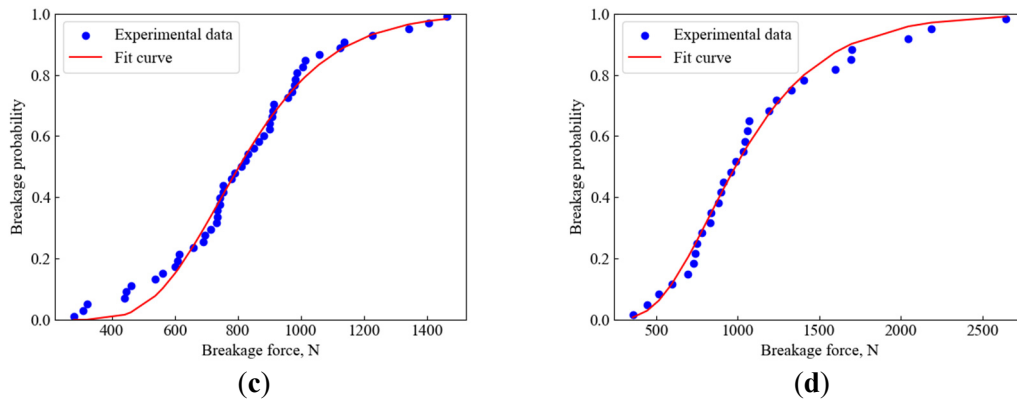
Figure 5. Distribution of breakage probability and compressive strength for DRI with different particle sizes: (**a**) 8–10 mm; (**b**) 10–12.5 mm; (**c**) 12.5–14 mm; (**d**) 14–16 mm.

The breakage probability $P(E)$ of DRI with different particle sizes and the fitting curves based on specific breakage energy are shown in Figure 6. Similarly, as the DRI particle size increases, the specific breakage energy corresponding to the same breakage probability decreases. Compared with Figure 4, it can be seen that under the same particle size and breakage probability, the specific breakage energy of pellets is higher than that of DRI.
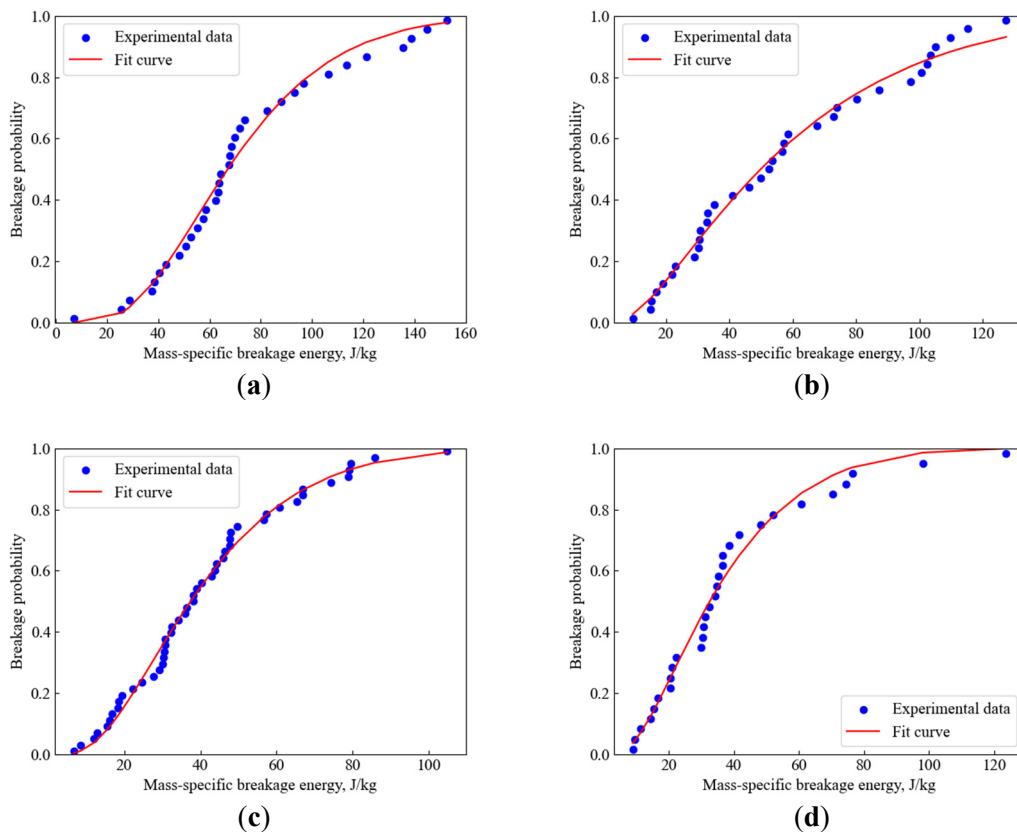

Figure 6. Distribution of breakage probability and specific breakage energy for DRI with different particle sizes: (**a**) 8–10 mm; (**b**) 10–12.5 mm; (**c**) 12.5–14 mm; (**d**) 14–16 mm.

Table 3 shows the average particle size, α_F, σ_F, α_E, σ_E and R^2 values for pellets of different particle sizes. Where α_F is the fitting parameter for breakage probability $P(F)$ using compressive strength, and σ_F represents the standard deviation of breakage probability $P(F)$ using compressive strength. α_E is the fitting parameter for breakage probability $P(E)$ using specific breakage energy, and σ_E represents the standard deviation of breakage probability $P(E)$ using specific breakage energy.

It can be observed from Table 3 that the model function exhibits a good fitting effect. α_F showing a positive correlation with particle size. In contrast, α_E is negatively correlated with particle size, indicating that larger pellets tend

to fracture at lower specific energies, as results reported by Tavares (2004) [16]. Additionally, neither σ_F nor σ_E demonstrates a significant relationship with pellet size, a finding similar to that in Reference [17].

Table 3. Summary of breakage characteristic parameters for pellet in four particle size ranges.

Pellet Size Range, mm	Average Size, mm	α_F, N	σ_F	R^2	α_E, J/kg	σ_E	R^2
10–12.5	11.853	2945.41	0.297	0.975	314.47	0.586	0.987
12.5–14	13.453	3322.14	0.250	0.980	219.11	0.502	0.991
14–16	15.126	3662.08	0.229	0.970	158.12	0.438	0.983
16–20	16.635	4422.22	0.186	0.984	105.45	0.610	0.973

Table 4 shows the average particle size, α_F, σ_F, α_E, σ_E and R^2 values for DRI with different particle sizes. It can be observed that both the α_F and α_E values of DRI are lower than those of pellets, indicating that DRI is more prone to breakage in the shaft furnace compared to pellets. Similarly, neither σ_F nor σ_E of DRI exhibits a significant relationship with particle size.

Table 4. Summary of breakage characteristic parameters for DRI in four particle size ranges.

DRI Size Range, mm	Average Size, mm	α_F, N	σ_F	R^2	α_E, J/kg	σ_E	R^2
8–10	9.580	596.62	0.337	0.986	83.83	0.599	0.985
10–12.5	11.625	686.51	0.480	0.991	62.3	0.964	0.990
12.5–14	13.257	803.82	0.283	0.987	46.81	0.728	0.992
14–16	14.810	986.80	0.421	0.989	40.7	0.824	0.979

Equation (6) is used to fit the experimental data of pellets and DRI with different sizes in Tables 3 and 4, as shown in Figure 7. Among them, A_F (N) and B_F (N/mm) are parameters obtained by fitting the experimental data, and d (mm) is the average particle size.

$$a_F = A_F + B_F d \tag{6}$$

It can be observed that compared with DRI, the compressive strength of the pellet increases more rapidly with the increase in particle size.
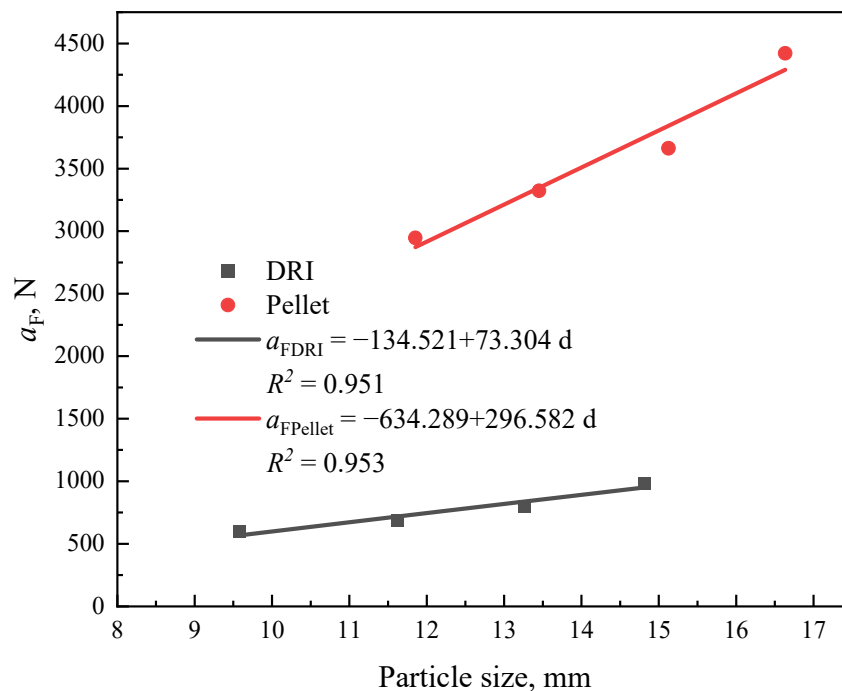

Figure 7. Fitting results of α_F and particle size of pellets and DRI.

According to Equation (7) [16], the α_E corresponding to various particle sizes can be predicted, and the results are shown in Figure 8. Among them, E_∞ (J/kg), d_0 (mm), and φ are parameters obtained by fitting experimental data, and d is the average particle size.

$$a_E = E_\infty \left[1 + \left(\frac{d_0}{d} \right)^\varphi \right] \tag{7}$$

Figure 8 shows the experimental data and the fitting curves for pellets and DRI in Tables 2 and 3. It can be observed that for both pellets and DRI, α_E decreases with increasing particle diameter, exhibiting a trend opposite to α_F. The reason is that although compressive strength increases with increasing particle diameter, this change is linear, whereas the specific breakage energy of pellets equals breakage energy divided by mass. Mass varies nonlinearly with particle diameter, rising more rapidly, resulting in decreased specific breakage energy with increasing particle diameter. Additionally, it can be noted that at identical particle diameters, α_E of pellets consistently exceed that of DRI, and this disparity progressively widens as particle diameter increases.
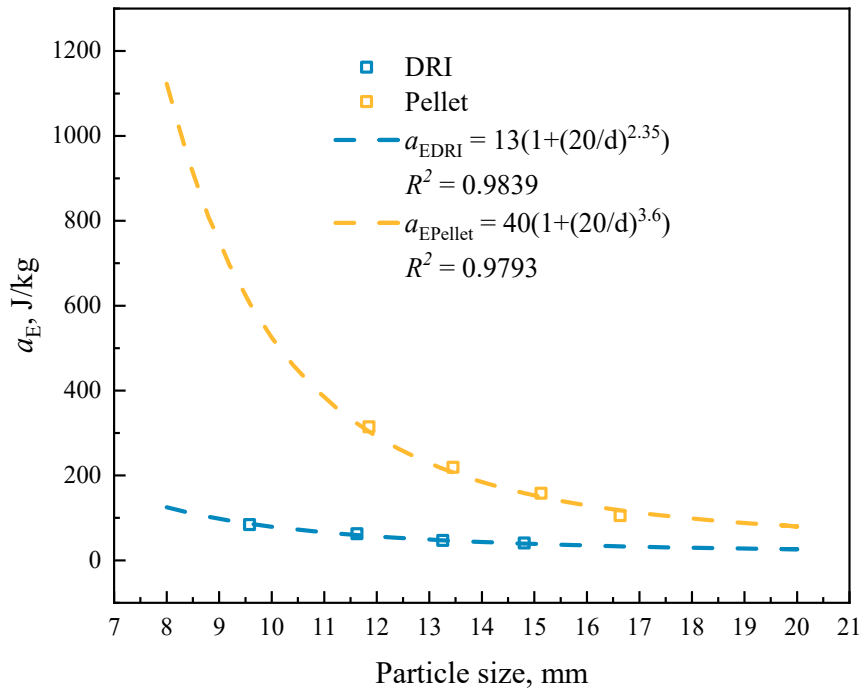

Figure 8. Fitting results of α_E and particle size of pellets and DRI.

The results of repeated compression tests for pellets and DRI are shown in Figure 9. It can be observed that the applied force gradually increases with the number of compression cycles for both materials. In terms of strain during compression, pellets fracture at the 5th compression cycle, while DRI only fractures at the 6th cycle, indicating that DRI can withstand greater compressive strain. However, pellets bear a higher force than DRI at a fixed compressive strain. For example, in the 4th compression cycle, the maximum compressive force of pellets is 3557 N, while that of DRI is only 719 N, suggesting that pellets exhibit smaller strain than DRI under the same applied force.
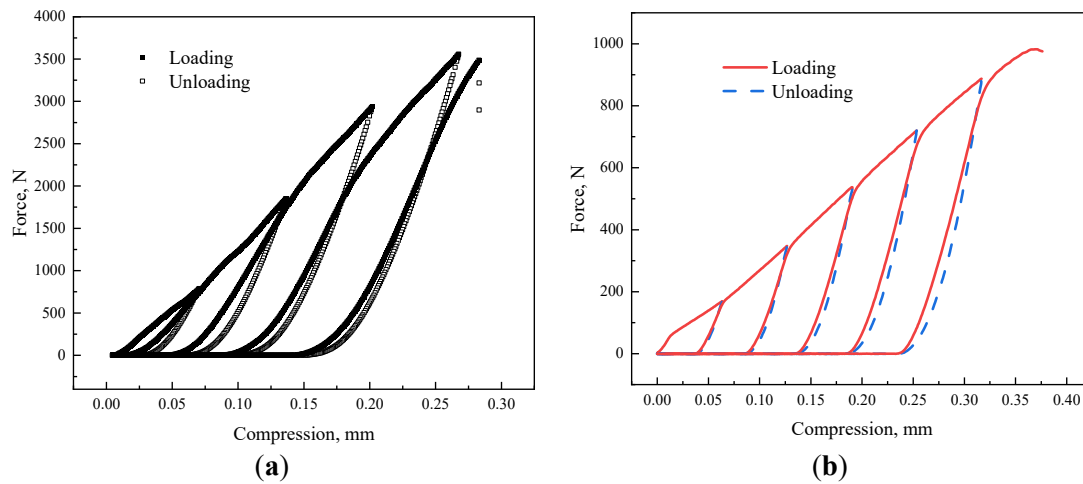
Figure 9. Force-displacement curves from repeated compression tests: (**a**) Pellets; (**b**) DRI.

3.2. Pore Distribution

Under hydrogen-based shaft furnace conditions, pellets undergo reduction by H_2 and CO, transitioning through the sequence $Fe_2O_3 \rightarrow Fe_3O_4 \rightarrow FeO \rightarrow Fe$. Simultaneously, free carbon is generated on the surface of DRI via cracking and carburization reactions of CH_4 and CO. This carbon combines with Fe to further form Fe_3C. The schematic diagram of the pellet-to-DRI evolution process is shown in Figure 10.
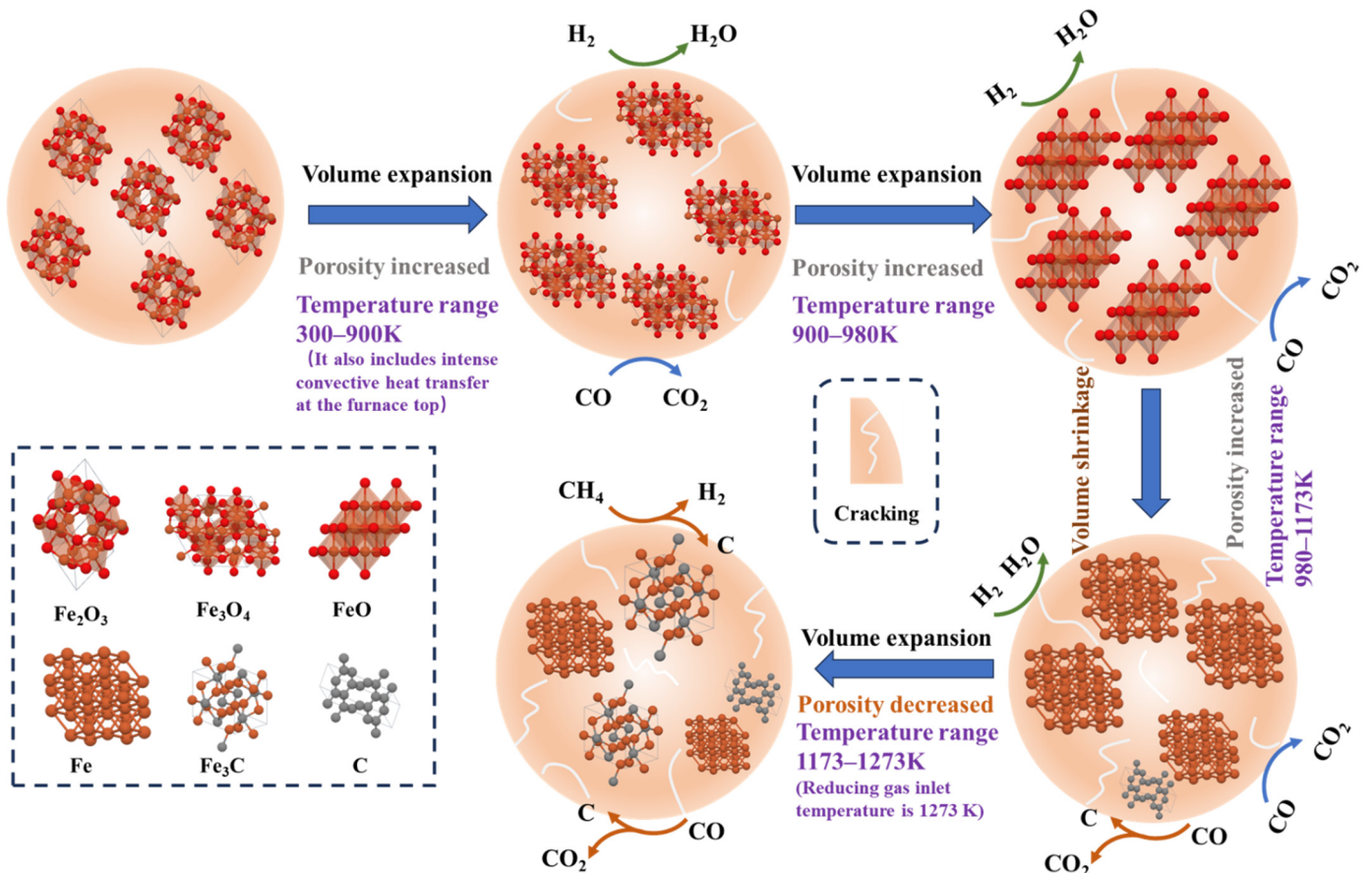
Figure 10. Schematic diagram of pellet transition to DRI under hydrogen-based shaft furnace conditions.

During the reduction from Fe_2O_3 to Fe_3O_4, the crystal structure transforms from a rhombohedral system to an inverse spinel structure of the cubic system. This transition triggers a reduction swelling, manifested as increased volume, higher porosity, and the appearance of cracks on the pellet surface. When further reducing from Fe_3O_4 to FeO, more significant changes in the crystal structure occur, exacerbating reduction swelling and making the cracks on the

pellet surface more pronounced. In the process of transforming FeO into Fe, the crystal structure changes from face-centered cubic to body-centered cubic, leading to reduction shrinkage and a decrease in volume. After this stage, most of the O elements in pellets are removed by H_2 and CO. Reduced mass loss of the O element plays a dominant role in pore formation during reduction; therefore, the internal porosity of pellets reaches its maximum at this stage. With the progression of the carburization reaction, on the one hand, part of the carbon exists as free carbon and fills the pores, resulting in a decrease in porosity; on the other hand, another part of the carbon combines with Fe to form Fe_3C. During this process, the crystal structure transforms into an orthorhombic system, causing a slight expansion in the volume of the pellet. It is worth noting that Fe_3C is more brittle than Fe [18–22]. The above series of transformations ultimately results in DRI exhibiting different characteristics from pellets. DRI has significantly higher porosity and lower compressive strength than pellets. This makes DRI more prone to breakage when subjected to impacts or collisions. In essence, the transformation of crystal structures and changes in pore structure during the reduction and carburization processes collectively affect the mechanical properties of the material, making the structural stability of DRI inferior to that of pellets and thus more susceptible to damage under external forces.

Figure 11 shows the pore size distribution functions and most probable pore sizes of pellets and DRI. As observed from Figure 11a, the pore volume of pellets increases sharply in the pore size range of 1600–4800 nm, rising from 5% to 97%, with no significant increase in pore volume for other pore sizes. For DRI, the pore volume gradually increases starting from a pore size of 36,000 nm, featuring a rapid growth zone in the range of 2480–4800 nm (increasing from 14% to 37%), followed by a steep increase from 46% to 95% at pore sizes of 350–1318 nm. Figure 11b illustrates the most probable pore sizes: pellets exhibit a single distinct peak at 3428 nm. DRI has two prominent peaks at 3431 nm and 831 nm, indicating smaller pore sizes in DRI compared to pellets. Pellets have uniformly distributed and relatively larger pores, whereas DRI contains micropores and fewer macropores.
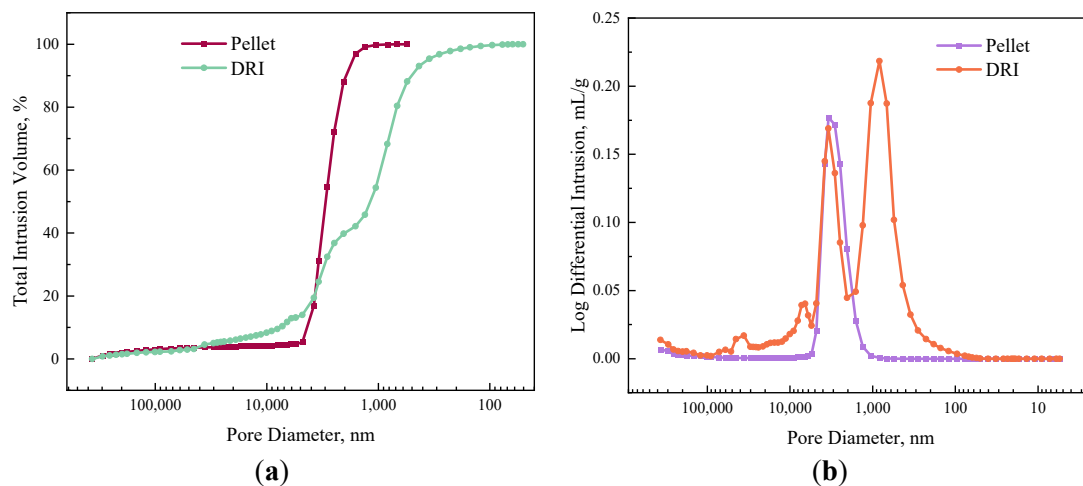

Figure 11. Comparison of pore diameters of pellets and DRI, (**a**) distribution function of pore diameters; (**b**) most probable pore diameters.

Figure 12 displays the pore distribution of pellets obtained via CT scanning, where Figure 12a and b are the original cross-sections of the edge and center, respectively, and Figure 12c and d show the pore distributions at the edge and center. The results in Figure 12 indicate that the pores in both the edge and center cross-sections of the pellets are dominated by macropores, consistent with the findings in Figure 10, and the pore distribution is relatively uniform.
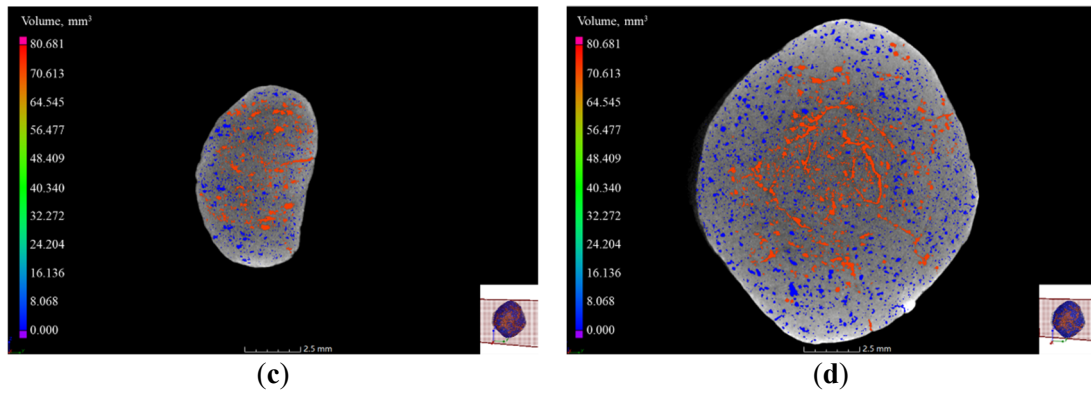

(**a**)   (**b**)

(c)   **(d)**
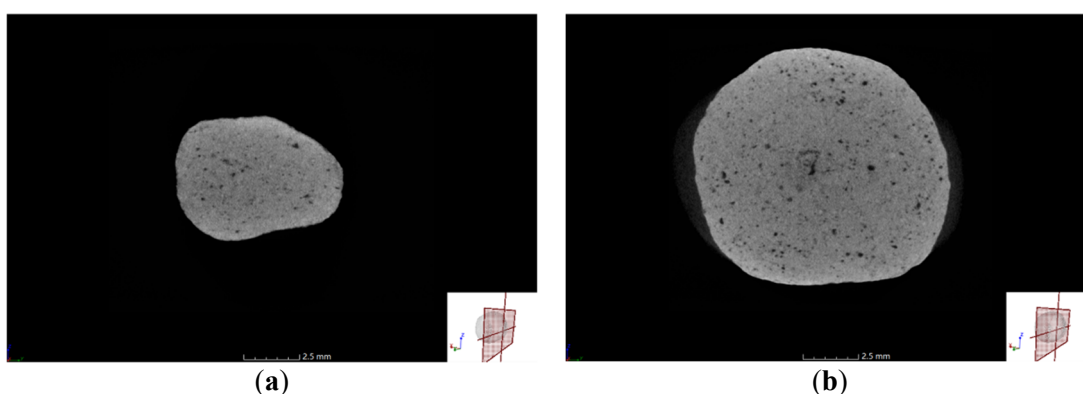
Figure 12. CT scanning results of pellets: (**a**) Original cross-section of the edge; (**b**) Original cross-section of the center; (**c**) Pore distribution at the edge; (**d**) Pore distribution at the center.

The CT scanning results of the DRI pore distribution are shown in Figure 13. The scanning results of DRI indicate that the edge cross-section is mainly composed of large-volume pores, while fine micropores dominate the central cross-section. Although the pore distribution is uneven, a clear comparison between Figures 12 and 13 reveal that pores in both the edge and center of DRI are more developed than those in pellets.
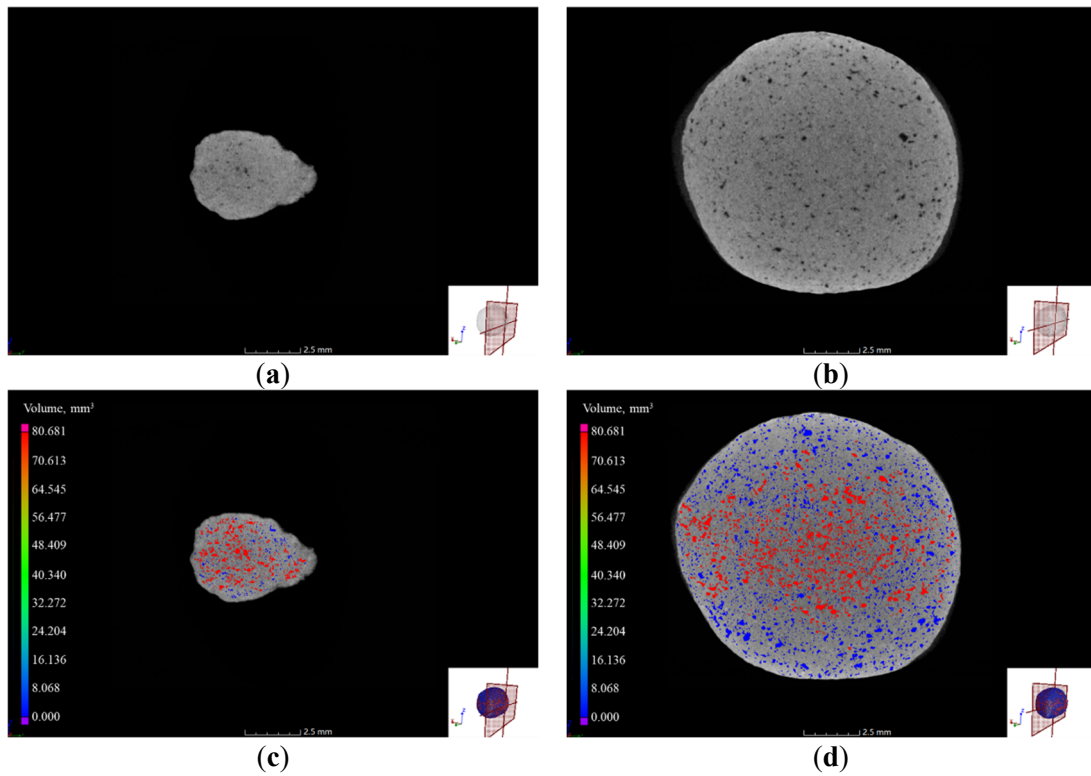

(a)   **(b)**

(c)   **(d)**

Figure 13. CT scanning results of DRI: (**a**) Original cross-section of the edge; (**b**) Original cross-section of the center; (**c**) Pore distribution at the edge; (**d**) Pore distribution at the center.

The porosity and tortuosity index (τ) of pellets and DRI are shown in Figure 14, with the calculation method of the tortuosity index described by Equation (8)–(10). A lower tortuosity index indicates a relatively smoother diffusion path and lower diffusion resistance. A lower tortuosity index allows H_2 to rapidly reach the center of the pellet, accelerating the H_2 reduction reaction process.

$$\xi = tortuosity = \frac{Actual \text{ distance traveled}}{shortest \text{ distance}} = \frac{\ell_e}{\ell} \tag{8}$$

$$\tau = \frac{\xi}{\sigma} \tag{9}$$

$$\sigma = f(\beta) \tag{10}$$

where ξ represents the tortuosity, σ is the constriction factor, and β is the area ratio.

As shown in Figure 14, pellets exhibit a compact structure with low porosity (only 22.3%), which is close to the results reported by Xu et al. (2020) [23], while DRI has a highly developed porous structure with a much higher porosity of 48.8%, which is close to the results reported by Tavares et al. (2025) [24]. It can also be observed that the tortuosity index of DRI is lower than that of pellets, indicating that gas diffuses more easily within DRI, which is related to its highly developed pores. Although the porous structure of DRI is beneficial for gas passage, the transformation from the compact structure of pellets to the porous structure of DRI leads to a decrease in strength, specifically manifested as the reduction of α_F and α_E in Section 3.1.
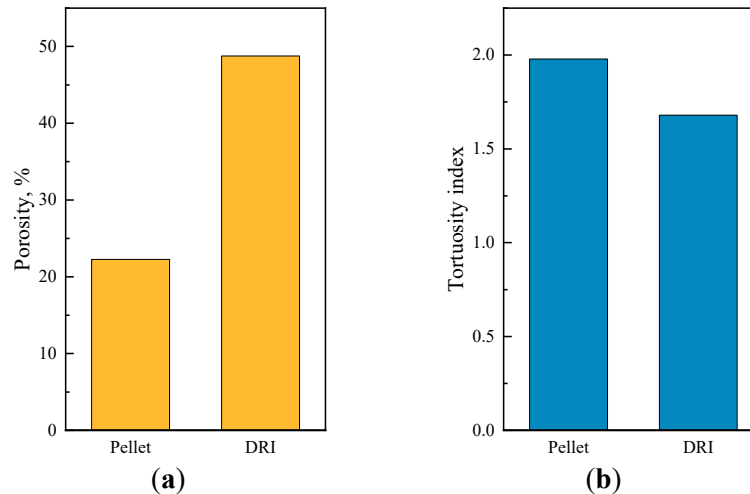

Figure 14. (**a**) Comparison of porosity between pellets and DRI; (**b**) Comparison of tortuosity index between pellets and DRI.

4. Conclusions

This study quantitatively investigated the differences in mechanical properties, such as compressive strength and specific breakage energy, between pellets and direct reduced iron (DRI) through compression tests. It analyzed the differences in pore structure and distribution between pellets and DRI. The main conclusions are as follows:

(1) Distribution function fitting was performed on the compressive strength and specific breakage energy of pellets and DRI with different particle sizes. The fitted fracture characteristic parameters α_F and α_E of DRI were lower than those of pellets at the same particle size, indicating that DRI is more prone to breakage under impact or collision.

(2) The compressive strength of pellets and DRI increased with particle size, while the specific breakage energy decreased with particle size. Variation curves of fracture characteristic parameters with particle size were obtained through formula fitting, which can be used to predict α_F and α_E of pellets or DRI with different particle sizes.

(3) Pellets were predominantly composed of large pores with uniform distribution, with a main pore size of 3428 nm. In contrast, DRI had predominantly small pores overall, with large pores mainly present in edge cross-sections and small pores in central cross-sections. The pore size distribution was uneven, primarily consisting of 3431 nm macropores and 831 nm micropores.

(4) DRI exhibited a highly developed porous structure with a porosity as high as 48.8%, while the porosity of pellets was only 22.3%. Additionally, DRI had a lower tortuosity index, meaning its porous structure facilitated gas diffusion but led to reduced strength.

Author Contributions

Ethics Statement

Not applicable.

Informed Consent Statement

Not applicable.

Data Availability Statement

Data will be made available on request.

Funding

Declaration of Competing Interest

The authors declare that they have no known competing financial interests or personal relationships that could have appeared to influence the work reported in this paper.

References

1. Holappa L. A general vision for reduction of energy consumption and CO2 emissions from the steel industry. *Metals* **2020**, *10*, 1117.
2. Flores-Granobles M, Saeys M. Minimizing CO_2 emissions with renewable energy: a comparative study of emerging technologies in the steel industry. *Energy Environ. Sci.* **2020**, *13*, 1923–1932.
3. Rechberger K, Spanlang A, Sasiain Conde A, Wolfmeir H, Harris C. Green hydrogen-based direct reduction for low-carbon steelmaking. *Steel Res Int.* **2020**, *91*, 2000110.
4. Duarte PE, Becerra J. Reducing greenhouse gas emissions with Energiron non-selective carbon-free emissions scheme. *Stahl und Eisen: Zeitschrift fuer die Herstellung und Verarbeitung von Eisen und Stahl* **2011**, *131*, 85.
5. Wagner D. Etude expérimentale et modélisation de la réduction du minerai de fer par l'hydrogène. PhD dissertation, Institut National Polytechnique de Lorraine-INPL, Nancy, France, 2008.
6. Lan C, Sun Q, Wang X, Liu C, Zhang W, Li Y, et al. Metallurgical properties evolution of coke oven gas zero reforming reduction pellet. *Iron Steel* **2024**, *59*, 1–16.
7. Barrios GKP, De Carvalho RM, Kwade A, Tavares LM. Contact parameter estimation for DEM simulation of iron ore pellet handling. *Powder Technol.* **2013**, *248*, 84–93.
8. Barrios GKP, Jiménez-Herrera N, Tavares LM. Simulation of particle bed breakage by slow compression and impact using a DEM particle replacement model. *Adv. Powder Technol.* **2020**, *31*, 2749–2758.
9. Tavares LM, Cavalcanti PP, De Carvalho RM, da Silveira MW, Bianchi M, Otaviano M. Fracture probability and fragment size distribution of fired Iron ore pellets by impact. *Powder Technol.* **2018**, *336*, 546–554.
10. Cavalcanti PP, Petit HA, Thomazini AD, de Carvalho RM, Tavares LM. Modeling of degradation by impact of individual iron ore pellets. *Powder Technol.* **2021**, *378*, 795–807.
11. Boechat FO, De Carvalho RM, Tavares LM. Simulation of mechanical degradation of iron ore pellets in a direct reduction furnace. *KONA Powder Particle J.* **2018**, *35*, 216–225.
12. Cavalcanti PPS. Calibration and Validation of a Mathematical Model of Degradation of Fired Pellets during Transportation and Handling. Master's thesis, Universidade Federal do Rio de Janeiro, Rio de Janeiro, Brazil, 2015.
13. Boechat FO, Rocha LTD, Carvalho RMD, Jung SM, Tavares LM. Amenability of Reduced Iron Ore Pellets to Mechanical Degradation. *ISIJ Int.* **2018**, *58*, 1028–1033.
14. Petit HA, Boechat FO, De Carvalho RM, Tavares LM. Analysis of impact of mechanical degradation of iron ore pellets on gas flow in a direct reduction furnace using simulation. *J. Mat. Res. Technol.* **2024**, *28*, 4540–4550.

15. Tavares LM, De Carvalho RM. Modeling breakage rates of coarse particles in ball mills. *Miner. Eng.* **2009**, *22*, 650–659.

16. Tavares L. Optimum routes for particle breakage by impact. *Powder Technol.* **2004**, *142*, 81–91.

17. Zhou Q, Pan Y, Zhu C, Wei Y, Yao F, Liu Z. Experimental study on strength distribution of brittle materials at quasistatic state. *J. China Coal Soc.* **2019**, *44*, 708–716.

18. Kim G, Pistorius PC. Strength of direct reduced iron following gas-based reduction and carburization. *Metallurg. Mat. Transact. B* **2020**, *51*, 2628–2641.

19. Deng X-J, Zuo H-B, Xue Q-G, Xue QG, Wang JS. Research on the reaction behavior of pellets in typical atmospheres of shaft furnaces: Reduction swelling and carbon deposition. *Powder Technol.* **2024**, *438*, 119629.

20. Huang Z, Yi L, Jiang T. Mechanisms of strength decrease in the initial reduction of iron ore oxide pellets. *Powder Technol.* **2012**, *221*, 284–291.

21. Kovtun O, Levchenko M, Oldinski E, Gräbner M, Volkova O. Swelling Behavior of Iron Ore Pellets during Reduction in H2 and N2/H2 Atmospheres at Different Temperatures. *Steel Res. Int.* **2023**, *94*, 2300140.

22. Yang J, Li L, Liang Z, Peng X, Deng X, Li J, et al. Direct reduction of iron ore pellets by H2-CO mixture: An in-situ investigation of the evolution and dynamics of swelling. *Mat. Today Commun.* **2023**, *36*, 106940.

23. Xu C, Zhang J, Liu Z, Wang Y, Li Z, Ma L. A Comprehensive Study of Pore Characteristics, Formation Mechanism and Reliability Analysis with Advanced Characterization Methods Within Pellets. *Transact. Indian Inst. Met.* **2020**, *73*, 2503–2510.

24. Tavares JHR, Da Luz JM, Ribeiro FF. Weathering impacts on iron ore pellets. *Caderno Pedagógico* **2025**, *22*, e16669–e16669.